CCD Standard Curve Fitting for Microarray Detection Base on Multi-Layer Perceptron

Zhenhua Gan, Dongyu He, Peishu Wu, Baoping Xiong, Nianyin Zeng, *Member, IEEE*, Fumin Zou, Feng Guo, Qin Bao, and Fengyan Zhao

***Abstract*—The Charge Coupled Device (CCD) scanner determines the concentration of the microarray by capturing the intensity of the fluorescent signal on the microarray in combination with the standard curve. Due to the characteristics of semiconductors, the CCD sensor in the scanner we designed suffers from saturation, the non-linear relationship between photoelectric response and the light intensity collected by CCD, which poses a challenge for fitting the standard curve of microarray scanner. The Least Squares Algorithm (LSA) still has a large relative error even in the case of high-order fitting, especially in the region of the fluorescence image with small gray level. However, the standard curve is critical to the highly accurate measuring of the instrument. In view of the poor curve fitting performance of LSA, Weighted Least Squares (WLS), and Penalized Least Squares (PLS), as well as the small dataset, this paper proposes the Multi-Layer Perceptron (MLP) neural network algorithm with the minimization of relative error as the constraint, which is applied to the standard curve fitting of the scanner. The gray-level of the fluorescent probe in detection image was obtained as the data set acquired by the microarray scanner at different exposure time. And the relative error and the standard deviation of the relative errors were used as evaluation indicators. In our experiments we compared the MLP neural network with relative error minimization as the constraint with the LSA and the MLP neural network with sum of square errors (SSE) minimization as the constraint. The experimental results show that the MLP neural network constrained by minimizing the relative error has good fitting performance for the standard curve of CCD scanner, with the maximum relative error of only 0.89% while the standard deviation of relative error of only 0.25%. It can be seen that this method provides a new approach for standard curve fitting of microarray scanner.**

***Index Terms*—Standard curve fitting, MLP, relative error, microarray, CCD scanner.**

I. Introduction

MICROARRAY has a powerful high-throughput detection capability for gene sequences, which makes it occupy an important position in the field of modern life sciences. With the rapid development of medical science and technology, microarray plays a more and more important role [1], [2]. However, the expression of gene sequences on microarray needs to go through a series of key experimental steps, including sample acquisition, PCR amplification, hybridization experiments, fluorescence scanning, meshing of microarray, probe segmentation, and sequence analysis [3]. It is well known that biochemical, mechanical, imaging [4], [5] and intelligent processing techniques [6] play a key role in the microarray scanner. Via the scanner, we are able to form a link between current biochemical reactions and computer data processing, thus facilitating the entire process of microarray information reading and processing. The main tasks for the detection process of the scanner are quantitative fluorescence excitation, photoelectric conversion and standard curve fitting of the scanner. The scanner emits light from the excitation source to irradiate the microarray, and the fluorescent markers in the chip then emit fluorescent signals, which are detected and recorded by the scanner.

As we known, the current microarray scanner is mainly divided into laser confocal scanner and Charge Coupled Device (CCD) scanner, where CCD scanners offer advantages such as simple construction, affordability, and high cost-effectiveness [7], [8], [9]. In our previous study [3], a highly sensitive microarray scanner utilizing CCD and LED was developed. However, due to the limited capacity of the corresponding charge potential in the CCD sensor's small-sized image elements, saturation frequently occurs, leading to non-linear characteristic in its response curve [10], [11]. Moreover, CCD sensor also exhibit dark current phenomena attributed to temperature and other factors, necessitating the mitigation of dark current effects on detection results through image processing. Therefore, failure to address the non-linear response characteristics of CCDs could adversely affect the scanner's detection accuracy if suitable standard curve fitting methods are not employed.

At the same time, the standard curve of the instrument is playing an important role in calibration, quality control and analysis of experimental results, which helps to ensure the accuracy and precision of the instrument. Meanwhile the calibration algorithm

Manuscript received 6 April 2024; revised 12 May 2024; accepted 3 June 2024. Date of publication 7 June 2024; date of current version 18 June 2024. This work was supported in part by the Natural Science Foundation of China under Grant 62073271, in part by the Fundamental Research Funds for the Central Universities of China under Grant 20720220076, in part by the Natural Science Foundation for Distinguished Young Scholars of the Fujian Province of China under Grant 2023J06010, in part by the Scientific Research Projects of the Science and Technology Department in Fujian of China under Grant 2023I0024 and Grant 2023J01952, in part by the Provincial Project of Education Department in Fujian of China under Grant JT180344, Grant FBJY20230078, and Grant FJJKBK23-045, and in part by the Scientific Research Projects in Fujian University of Technology under Grant KF-X19002, Grant KF-19-22001, Grant GY-H-21191, Grant GY-Z21049, and Grant GY-Z220210. *(Corresponding author: Nianyin Zeng.)*

Zhenhua Gan, Dongyu He, Baoping Xiong, Fumin Zou, Feng Guo, Qin Bao, and Fengyan Zhao are with the Fujian Key Laboratory of Automotive Electronics and Electric Drive, Fujian University of Technology, Fuzhou, Fujian 350118, China (e-mail: ganzh@fjut.edu.cn).

Peishu Wu and Nianyin Zeng are with the Department of Instrumental and Electrical Engineering, Xiamen University, Xiamen 361005, China (e-mail: zny@xmu.edu.cn).

Digital Object Identifier 10.1109/JPHOT.2024.3411396

has an irreplaceable role in hardware design and electronic processing [12]. The Least Squares Algorithm (LSA) has been widely used because of its advantages such as its simple method and high accuracy for fitting a small number of data sets [13], [14]. We had used the LSA to fit the standard curve of this microarray scanner. However, the LSA also fails to form an effective constraint on the relative error in the case of high-order fitting. Although a series of improved LSA fitting methods have been proposed, such as Weighted Least Squares (WLS) and Penalized Least Squares (PLS) [15], they also fail to form an effective constraint on the relative error, which leads to a larger relative error of the fitted standard curves in the region of smaller gray values.

Fortunately, with the rapid development of neural networks in recent years, increasing attention has been paid to the application of neural network algorithms for output prediction in various fields. F.B.M. Suah, et al., achieved a higher accuracy in predicting the pH of unknown buffer solutions by analyzing the input and output variables of multiple fiber optic pH sensors using a BP neural network model [16]. F. Hu, et al., analyzed and processed the signals collected by the acceleration sensors in Wireless Body Area network (WBAN) through BP neural network and applied it to the recognition of human body poses, meanwhile its recognition rate has a great improvement [17]. Y. Li, et al., applied a BP neural network to fit the relationship between the input frequency difference and the output pressure of a Surface Acoustic Wave (SAW) micro-pressure sensor, which was used to predict the output pressure of the micro-pressure sensor with high accuracy [18]. Meanwhile, deep learning has penetrated into different fields, including image recognition, signal processing, natural language processing [19], [20]. The Multi-Layer Perceptron (MLP) neural network algorithm is a typical neural network algorithm in deep learning. MLP is a feed-forward neural network consisting of one or more input layers, one or more hidden layers, and one output layer. Each layer is fully connected to the next and transformed by a nonlinear activation function. The hidden layer of the MLP allows the network to learn and represent nonlinear relationships, which makes it capable of solving more complex problems. At the same time, the MLP neural network is able to learn more features despite the small number of datasets. This advantage is crucial for us to fit the standard working curve of the scanner. Gongbo Li, et al., proposed an artificial sideline attitude sensing method based on a hybrid activation function-multilayer perceptron model for identifying various attitudes of underwater vehicles [21]. Fermín Rodríguez, et al., used MLP to develop a very short-term temperature predictor to make photovoltaic power generation more reliable [22]. Various parameters such as tensile strength, tensile modulus, flexural yield strength, flexural yield modulus, Young's modulus, modulus of elasticity and density of PMC/plastic composites were evaluated by T. Sathish, et al., using the MLP [23]. It can be seen that the application of MLP neural networks to analyze the relationship between inputs and outputs in various domains is universal and reliable. Therefore, we propose a MLP neural network algorithm with relative error minimization and apply it to standard curve fitting for the microarray scanner. In terms of MLP training constraints selection, we use the minimization of the sum of squared errors (SSE) as the constraint, and find that the maximum relative error of its fitted standard curve is still at a large value. Then we use the minimization of the relative error as the constraint to train the MLP neural network model, and achieved better results.

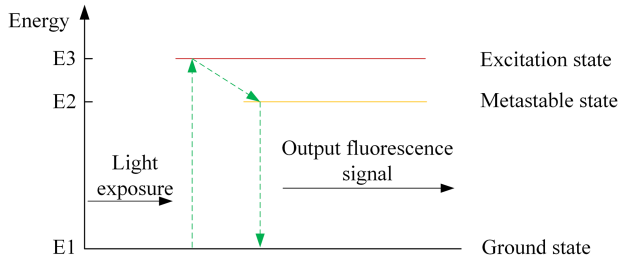

Fig. 1. Schematic diagram of fluorescence generated by excited electron transitions.

In view of the nonlinearity response of CCD microarray scanner in practice, we propose an MLP neural network based on the relative error minimization for standard curve fitting of scanner in this paper. This MLP has the advantage of light weight and high accuracy. The experimental results show that the standard curve fitted using the MLP neural network with relative error minimization as the constraint is superior to the LSA both in terms of the relative error and the standard deviation of the relative error.

The rest of the paper is organized as follows: a brief introduction to the fluorescence detection principle, scanner-related knowledge, LSA, WLS and PLS in Section II; the description of MLP in Section III; fitting experiments to the data using LSA, WLS, PLS and MLP with different constraints, respectively, in Section IV; and a summary and discussion of our work in Section V.

II. Detection Principles and Equipment

In this section, the principle of quantitative fluorescence detection is briefly introduced at first. Then the CCD photoelectric conversion and its shortcomings are described as well as the scanner we designed. Finally, the knowledge about LSA, WLS and PLS are explained.

A. Quantitative Fluorescence Detection

Quantitative fluorescence detection is an analytical method that determines the number of the target molecules based on the fluorescence signal emitted by the target molecules under irradiation at a specific wavelength. The concentration of the target molecules is calculated by exciting the target molecules in the sample so that it is in an excited state and emits a fluorescent signal. The process of luminescence can be explained in terms of particle jumps, as shown in Fig. 1.

Firstly, the particle absorbs energy under the irradiation of light at a specific wavelength and jumps from the ground state to the excited state. Then, it goes through the non-radiative jump to the metastable state, and finally, it returns from the metastable state to the ground state and emits fluorescence signal. The detector calculates the current concentration of a target molecule by capturing and recording the intensity of these fluorescent

signals and combining them with a standard curve of known concentration.

Fluorescence quantitative detection has the advantages of high sensitivity, high selectivity, multi-channel detection and real-time monitoring. Anthocyanin-3 (Cy3) is commonly used as the fluorescent dye in many microarray analyses to label specific biomolecules, which fluoresce at the same time as Cy3-labeled DNA probes. These excited fluorescence signals can be effectively captured by a specialized fluorescence scanner [24], [25], [26]. Therefore, our scanner in [3] is used to determine the current concentration by measuring the image gray value of the fluorescence signal in Cy3 at different irradiation time combined with the standard curve of the scanner.

B. Principle of CCD Photoelectric Detection

CCD sensor has a wide range of applications in the inspection field, especially in weak fluorescence detection. [27], [28]. It is easy to measure the intensity of the fluorescent signals by capturing the fluorescent image. When the photons hit the surface of the CCD sensor, it could excite the electrons and creates electron-hole pairs in proportion. And we can describe this efficiency of PV conversion in terms of the quantum efficiency QE, which is defined as

$$QE = \frac{N_e}{N_{photon}} \tag{1}$$

where N_e denotes the number of electrons produced by photoelectric conversion, N_{photo} denotes the number of incident photons.

In CCD sensor, these electrons are collected in the presence of the electric field into an array of many charge-coupled units which are called pixels. The amount of charge, denoted as Q_{pixel}, in each pixel cell is proportional to the energy of the incident photon. The charge storage equation is as follows

$$Q_{pixel} = k_\beta \, E_{photon} \tag{2}$$

where k_β denoted as a constant for the proportionality of the energy of the incident photon being converted to charge, while E_{photon} denoted as the energy of the incident photons.

These charges are transferred to the outputs, where the amplifier amplifies could convert the charge signals into voltage signals that could be measured. In this way the charge accumulated in each cell, Q_{pixel}, are converted into the analog voltage, correspondingly. Finally, via Analog-to-Digital Converter, the analog signals can be converted to the digital signals, and it is not inevitable to see that theoretically the intensity of the light response of the CCD is proportional to the light intensity.

Unfortunately, the dark current is unavoidable for semiconductor including CCD sensor. And the CCD's dark current is generated by the movement of electrons caused by thermal motion due to temperature. Very badly, the dark current of the CCD will produce a lot of noise in the image, which seriously degrades its quality, especially under the long exposure condition. In CCD sensor, one source of dark current is the thermal excitation effect of electrons, which creates carriers at zero bias. Another, the semiconductor impurities can also lead to the generation of carriers, thus generating dark current. Semiconductor impurity-induced electron-hole pair generation is usually temperature dependent, and high temperatures increase the rate of impurity-induced carrier production and thus dark current, which is defined in following

$$I_{dark} = I_0 \left(e^{\left(\frac{-E_a}{kT}\right)} - 1 \right) \tag{3}$$

where I_0 is the material-specific saturation current, E_a is the energy required for an electron to jump from the valence band to the conduction band, k is the Boltzmann constant, and T is the temperature.

The (3) expresses the exponential relationship between the dark current and the temperature of CCD sensor, indicating that the dark current increases with the temperature. Therefore, we need to reduce the temperature of the CCD sensor to eliminate the effects of dark current.

In CCD detection system, the dark current accumulated by the CCD's pixel varies with the exposure time. In our scanner, we assume that E_c is the illumination of the pixel while t is the exposure time. Then the integral gray-level of the CCD's pixel, denoted as H_t where $H_t = E_c t$, could be expressed by polynomials, and the relationship between grayscale and H_t can be defined as follows [10]

$$grayscal\ (H_t) = \sum_{n=1}^{N} c_n H_t^n + I_{dark}\,(0,t) \tag{4}$$

where $I_{\mathrm{dark}}(0,t)$ is the accumulation of dark current of each pixel at the exposure time of t, c_n is the fitting coefficient of the polynomial.

In general, the background noise introduced by dark current can be effectively eliminated by phase-subtracting CCD images taken at the same integration time (exposure time) under illuminated and non-illuminated conditions. Firstly, we could acquire two images, and one taken under illuminated conditions while another taken under non-illuminated conditions. Then, these images are preprocessed to ensure that they have the same size and gray scale range. Next, the image under illuminated condition is subtracted from the image under the non-illuminated condition, which could eliminate the background noise introduced by the dark current and obtain a new image that does not contain the effects of dark current signals.

C. CCD Saturation Phenomenon

Although the photoelectric response of CCD pixel is theoretically proportional to its collected intensity, in practice this is not the case. In CCD sensor, the photosensitive element absorbs photons and generates electron-hole pairs, these carriers are collected in the storage unit. However, when the light intensity is too high or the duration is too long, the rate of carrier production in the photosensitive element exceeds the collection capacity of its storage. The number of electron-hole pairs generated by the photosensitive element exceeds the capacity limit of the storage cell, resulting in saturation of the charge in the storage cell and the inability to continue accumulating charge. In this case, even though photons are still acting on the photosensitive element,

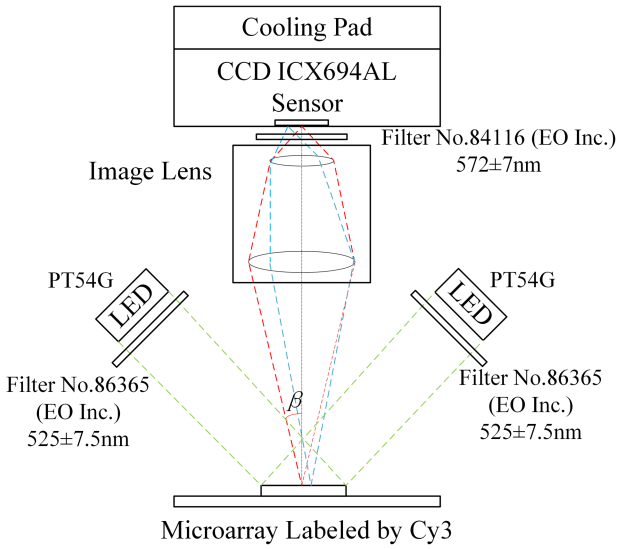

Fig. 2. Structure of CCD scanner for microarray biochip.

no additional charge accumulation can be generated because the charge has reached its maximum capacity, called saturation. This phenomenon makes the response of the CCD chip non-linear and loses the detailed information in the original image. Therefore, the nonlinearity of the CCD photoelectric response makes it more important to fit a standard curve, and poses a challenge in fitting the standard curve.

D. Microarray Scanner Based on LED and CCD

We had designed a microarray scanner based on LED and CCD in [3]. The scanner adopts wide-grid optical imaging technology to realize multi-pixel parallel acquisition, which greatly improves the detection speed of microarray. Its schematic structure is shown in Fig. 2.

The CCD camera we used in the scanner is ICX694AL, with a pixel count of 6.09 million and each pixel size of 4.54 μm $\times$ 4.54 μm. This CCD has a full-well capacity of 2×10^4 electrons and a photoelectric conversion efficiency of up to 75% at 600 nm. Especially under the condition of -35 °C, its dark current noise is 6×10^{-4} e/pixel·s [29]. At the same time, the high-power LED we used in the scanner is PT54G, with a green light at the center wavelength of 525 nm, a light surface of 5.4 mm^2, and a green radiation of up to 3200 lm. It can provide sufficient power for effectively exciting Cy3 fluorescent groups by combining high-power LED with narrowband filters [3]. Due to the OD6 optical narrowband filter No.86365 from Edmund Optics Inc. (EO Inc.), with a wavelength of 525 $\pm$ 7.5 nm, we combined this filter with PT54G to emit 1900 lm of green light at approximately 525 nm. Due to the narrow Stokes shift of absorption and emission of Cy3, which is about 20 nm, and its absorption peak is around 550 nm and emission peak is around 570 nm [3], we used the No.84116 filter with a wavelength of 572 $\pm$ 7 nm to collect the fluorescence information of Cy3.

Assuming S_p is the CCD pixel area and S_{ex} is the square of the probe on the microarray, then $S_{ex} = S_p \times \rho_{op}$, where ρ_{op} is the optical magnification obtained by assembling an image lens and a 573 nm filter.

Subsequently, the number of photons excited by S_{ex} captured every pixel on the CCD can be expressed as:

$$Q_{em} = \rho_{em} \frac{1-\cos\beta}{2} Q_{ex},\ \beta = \sin^{-1}(NA) \tag{5}$$

$$Q_{ex} = f \cdot S_{ex} \cdot C_{ex} \cdot t \tag{6}$$

where ρ_{em} denotes the transmittance obtained by assembling an image lens and the 572 nm filter, f represents the photon rate generated by each Cy3 fluorescent molecule, C_{ex} is the concentration of fluorescent dye, t is the CCD exposure time, NA is the numerical aperture of the lens, and the number of fluorescent photons excited by Cy3 dye in S_{ex} is denoted as Q_{ex}.

At the same time, we assumed that the quantum effect of CCD is $\S_{CCD}$, the photoelectric number Q_{pix} converted from Cy3 photon Q_{em} is represented as follows:

$$Q_{pix} = \S_{CCD} \cdot Q_{em} = \S_{CCD} \cdot f \cdot t \cdot C_{ex} \cdot \rho_{op} \cdot S_{pix} \tag{7}$$

The pixel unit of CCD ICX694AL is Sp = 4.54 μm $\times$ 4.54 μm, with the valid pixels of $N_p = 2750 \times 2200$ and the target surface of $S_0 = 9.99$ mm $\times$ 12.49 mm. The transmittance of our scanner is $\rho_{em} = 83.7\%$, with $\beta = \sin^{-1}(0.22) = 12.7°$. Assuming optical magnification $\rho_{op} = 2.2$, then $S_{ex} = 10\ \mu\text{m} \times 10\ \mu\text{m}$. Hence, the detection limit of CCD can be defined as the number of photoelectrons $Q_{pix(\min)}$, which can be solved according to (6) and (7), as well as assuming that the minimum number of photoelectrons corresponding to Cy3 is $Q_{cy3(\min)}$, as follows:

$$Q_{cy3(\min)} = \frac{Q_{pix(\min)}}{\S_{CCD} \cdot \rho_{em} \cdot \frac{1-\cos\left(\sin^{-1}(NA)\right)}{2}} = 131.8 \cdot Q_{pix(\min)} \tag{8}$$

where $\rho_{em} = 83.7\%$, $NA = 0.22$, and $\S_{CCD} = 0.74$.

Finally, we have used this scanner to take pictures of the Cy3 calibration chip of Beijing CapitalBio Nanobrite^{TM} with the LED exposure integration time of 30s, and we have obtained the image shown in Fig. 3.

In Fig. 3, the response image is showed a very obvious saturation in many probes some columns. This phenomenon is due to the internal photoelectric effect of the CCD pixel increases with continuous exposure, which causes the nonlinear in its output signal. However, the accuracy of fluorescence excitation measurements on microarray is strongly dependent on the response of the CCD sensor, and the standard curve of the CCD scanner is importance to overcome the nonlinear characteristics of the microarray.

E. Method of LSA, WLS and PLS

Nowadays, the linear regression modeling is getting lots of applications in various fields to solve functional relationship problems. One of the common mathematical optimization algorithms is LSA, which is often used to determine a function coefficient that best describes the relationship between data points by fitting the values to those data points. LSA has been

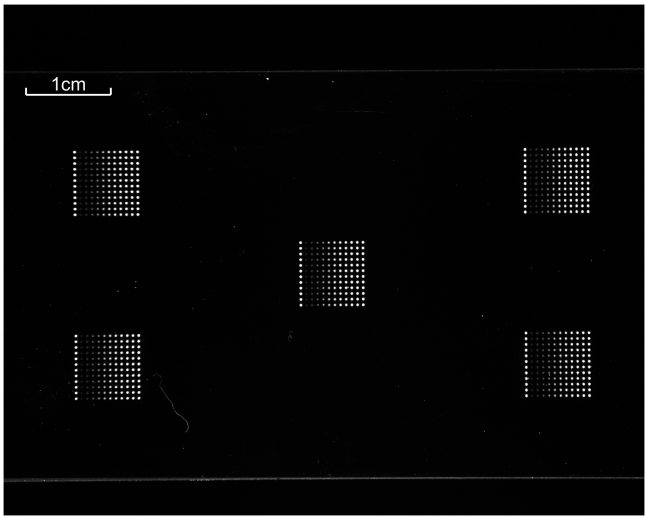

Fig. 3. Image of the Cy3 calibration chip of Beijing CapitalBio Nanobrite™ at LED integration time of 30 s.

utilized in diverse studies to tackle specific challenges across various fields. For instance, in wireless sensor networks, it was employed to estimate communication time offset and skewness, thus improving global time synchronization via compensation algorithms [30]. In hyperspectral remote sensing, LSA facilitated the derivation of noise parameters for spectral sensors, aiding in noise estimation [31]. Similarly, LSA was applied to optimize the active muscle force-length model through curve-fitting, enhancing its precision and utility [32].

The purpose of data fitting using LSA is to obtain an optimal regression function that minimizes the SSE [33]. We can assume that the values of the actual data points are (*xi, yi*), and the regression function, denoted as *y*, obtained by LSA is defined as follows

$$y = f(x, \beta) \tag{9}$$

where β is the function coefficient. In (5), the goal of LSA is to find the value of β that minimizes the error e_i, which is expressed as follows

$$e_i = yi - f(xi, \beta) \tag{10}$$

Therefore, we can define the SSE, which could be denoted as *S,* in following

$$S = \sum_{i=1}^{n} ei^2 = \sum_{i=1}^{n} (yi - f(xi, \beta))^2 \tag{11}$$

The process of solving the partial derivation of (9) for β is shown in (12).

$$\frac{\partial S}{\partial \beta j} = -2 \sum_{i=1}^{n} ei \frac{\partial f(xi, \beta)}{\partial \beta j} \tag{12}$$

When the partial derivatives in (8) are minimized, we can assume that the best regression function coefficients are currently obtained.

According to previous theory and derivation, we can find that the LSA optimization idea is to minimize the SSE between the actual data and the predicted values. However, it is not able to constrain the relative error effectively and this drawback makes the curve fitted by the LSA have a large relative error in the region where the detection value is small, which significantly affects the detecting accuracy of the CCD scanner.

Since the significant relative error in LSA, some improved LSA have emerged such as WLS and PLS. WLS assigns weights to each data point to make the final fitted curve closer to the actual value, so we can set the weight matrix as follows:

$$W = \begin{bmatrix} \omega_1 & 0 & \dots & 0 \\ 0 & \omega_2 & \dots & 0 \\ \dots & \dots & \dots & \dots \\ 0 & 0 & \dots & \omega_n \end{bmatrix} \tag{13}$$

where ω_i (i = 12, …,n) represents the weight of each data point.

Therefore, the SSE of WLS can be rewritten as follows:

$$S = \sum_{i=1}^{n} \omega_i ei^2 = \sum_{i=1}^{n} \omega_i (yi - f(xi, \beta))^2 \tag{14}$$

Subsequently, PLS adds L2 regularization term during the fitting process to prevent overfitting, which improves the fitting results with strong generalization ability. The goal of PLS curve fitting is to minimize the following functions:

$$L(\beta) = \|y - x\beta\|_2^2 + \delta\|\beta\|_2^2 \tag{15}$$

where δ represents the regularization parameter.

Nevertheless, WLS and PLS have made a series of improvements to optimize the fitting results compared to LSA, but their maximum relative error still cannot be within our acceptable range.

III. Method of MLP

The LSA cannot effectively constrain the relative error of the fitted curves, so we urgently need a new method to fit the standard curves of CCD scanner to improve the accuracy for detecting the microarray. Based on the relative error minimization, we propose a MLP neural network to try and solve the problem. The MLP is a feedforward neural network composed of one or more hidden layers and an output layer. Its each layer consists of multiple neurons with learnable weights and an activation function, and neurons across different layers in the MLP are fully interconnected, allowing the network to learn the nonlinear relationship between input and output by adjusting weights continuously.

The MLP training process utilizes backpropagation to update inter-layer weights by propagating the relative error of each output round backward, enabling accurate predictions with minimal data and demonstrating strong generalization capabilities. Consequently, we employed the MLP structure with relative error minimization, to fit the standard curve of the microarray scanner.

The MLP neural network model we designed consists of an input layer, a hidden layer with *m* neurons, and an output layer as shown in Fig. 4.

We use the sigmoid function as the activation function for the hidden layer, and we assume that *P* is denoted as the input

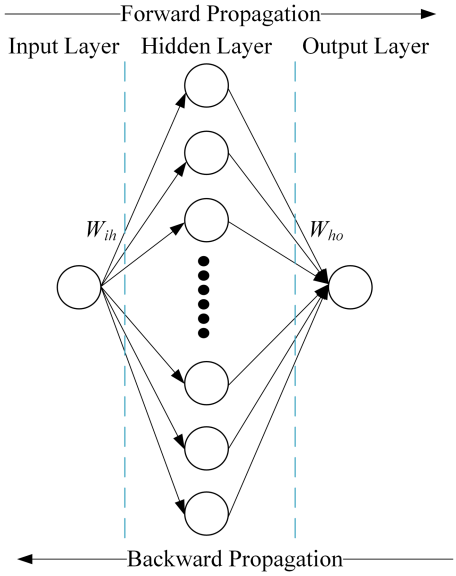

Fig. 4. Structure of MLP neural network model, where the black circle represents the neuron, W_{ih} represents the direct weight between the input layer and the hidden layer, and W_{ho} represents the weight between the hidden layer and the output layer.

information of the neuron, Q is denoted as the output information of the neuron, W_{ih} is denoted as the corresponding connection weights between the input layer and the hidden layer, W_{ho} is denoted as the corresponding connection weights between the hidden layer and the output layer, K_h is denoted as the threshold value of the neuron within the hidden layer, $f_h(x)$ expressed as its activation function, and K_o is expressed as the neuron threshold assumption within the output layer.

Since there is only one neuron in the input layer in our MLP neural network model, the input and output of the input layer can be represented as follows

$$P_i = Q_i \tag{16}$$

According to the weights and thresholds between the input and hidden layers, the input of the neurons in the hidden layer and the output of the neurons in the hidden layer can be expressed as

$$P_{hx} = W_{ih} \times Q_i,\ x = 1, 2, \ldots, m \tag{17}$$

$$Q_{hx} = f_h\left(P_{hx} - K_{hx}\right), x = 1, 2, \ldots, m \tag{18}$$

The output of the output layer is obtained by the connection weight coefficients between the hidden layer and the output layer of the MLP as well as the neuron thresholds, so that the input and output expressions of this output layer can be deduced. As there is only one neuron in the output layer in our MLP neural network, the input expression of the output layer and the output expression of the output layer can be represented as follows

$$P_o = \sum_{x=1}^{m} W_{ho} \times Q_{hx},\ (x = 1, 2, \ldots, m\ ) \tag{19}$$

$$Q_o = P_o - K_o \tag{20}$$

where m is the number of neurons in the hidden layer.

The relative error between the output value and the actual value is calculated during the back propagation process of the MLP neural network, and the weights between the layers are constantly updated by back propagation. This makes the relative error of the output value in the neural network constantly converge to 0 after each weight update. Therefore, in the back-propagation process of MLP neural network, we assumed that the output of our MLP neural network for n input values is F_x and the actual value is d_x where $x = 12, \ldots$,n. So the output of MLP neural network, expressed as F_x, can be represented in following

$$F_x = \left(P_o - Ko\right) \tag{21}$$

And the relative error can be expressed as

$$E_x = \left|\frac{F_x - d_x}{d_x}\right|, x = 1, 2, \ldots, n \tag{22}$$

In the gradient descent-based strategy, the connection weights of neurons between different layers are adjusted along the negative gradient of the relative error. According to the relative error of the current output and the learning rate η, the connection weight changes between the hidden and output layers can be derived as shown in (23) with (24).

$$\Delta W_{ho} = -\eta \frac{\partial E_x}{\partial \Delta W_{ho}} \tag{23}$$

$$\frac{\partial E_x}{\partial \Delta W_{ho}} = \frac{\partial E_x}{\partial F_x} \cdot \frac{\partial F_x}{\partial P_o} \cdot \frac{\partial P_o}{\partial \Delta W_{ho}} \tag{24}$$

So the (25) could be evident from (19).

$$\frac{\partial P_o}{\partial \Delta W_{ho}} = Q_{hx} \tag{25}$$

Since the sigmoid activation function is well characterized, it can be expressed as follows

$$f'(x) = f(x)\left(1 - f(x)\right) \tag{26}$$

Therefore, the (27) also can be deduced from (21) and (22).

$$g = -\frac{\partial E_x}{\partial F_x} \cdot \frac{\partial F_x}{\partial P_o} = F_x\ \left(1 - F_x\right)\left(d_x - F_x\right) \tag{27}$$

And the (23) could be rewritten as (28), too.

$$\Delta W_{ho} = \eta g Q_{hx} \tag{28}$$

Similarly, we can derive the expression for the weight change of the connection between the input layer and the output layer, as shown in (29), as well as the derivation of (30) and (31).

$$\Delta W_{ih} = -\eta \frac{\partial E_x}{\partial \Delta W_{ih}} \tag{29}$$

$$l = -\frac{\partial E_x}{\partial Q_{hx}} \cdot \frac{\partial Q_{hx}}{\partial P_{hx}} = -\sum_{x=1}^{m} \frac{\partial E_x}{\partial P_o} \cdot \frac{\partial P_o}{\partial Q_{hx}} f'\ \left(P_{hx} - K_{hx}\right)$$

$$= Q_{hx}\ \left(1 - Q_{hx}\right) \sum_{x=1}^{m} W_{ho} g \tag{30}$$

$$\frac{\partial P_{hx}}{\Delta W_{ih}} = Q_i \tag{31}$$

Finally, we can rewrite (29) into (32) as follows

$$\Delta W_{ih} = \eta l Q_i \tag{32}$$

During the training process of the MLP neural network, the weights between the hidden and output layers and between the input and hidden layers are continuously updated.

In practice, the weights between the hidden and output layers, as well as between the input and hidden layers, are continuously updated during the training of the MLP neural network. And the weight update between the hidden and output layers is shown in (33), while the weight update between the input and hidden layers is shown in (34).

$$w_{ho}\,(n+1) \;= w_{ho}\;(n) + \Delta w_{ho} \tag{33}$$

$$w_{ih}\,(n+1) \;= w_{ih}\;(n) + \Delta w_{ih} \tag{34}$$

Where $\omega\ w_{ho}(n+1)$ denoted as the weight between the hidden layer and the output layer at the n+1st round of training, $w_{ho}(n+1)$ denoted as the weight between the input layer and the hidden layer at the n+1st round of training, while $w_{ho}(n)$ denoted as the weight between the hidden layer and the output layer at the nth round of training, $w_{ih}(n)$ denoted as the weight between the input layer and the hidden layer at the nth round of training.

The training process of the MLP neural network is to modify the neuron weights in each layer by forward and backward propagation of the signal, and the model weight file with the smallest relative error would be saved during the MLP neural network training process, which makes it easy to use this weight file to generate the corresponding output signals based on the current input values.

IV. Experiment

In this section, the dataset acquired by CCD scanner is described at first. Then this dataset is used to fit the standard curve via LSA, MLP with the constraint in minimization of the SSE, and MLP with the constraint in minimization of relative error, respectively. Finally, the maximum relative error and the standard deviation of the relative error were used as evaluation metrics to compare their fitting performance.

A. Dataset and Evaluation Index

The dataset utilized in the experiments was obtained by a CCD scanner as described in Fig. 2, and the fluorescence images were captured from 1s to 30s with the interval of 1s, resulting in a total of 30 images, which demonstrated the grayscale information corresponding to the fluorescence intensity. The grayscale is obtained as an example for an image with the integration time of 30s, as shown in Fig. 5.

Their grayscale information from all marker points in the sixth column (indexed from 0 to 11, left to right) of each image have been collected, and their average value could be calculated to represent the grayscale at each integration time.

Then, we obtained a total of thirty data-points through actual measurements, and we calculated the difference between each adjacent point. The results are shown in Table I. From Table I, we can conclude that there is a significant saturation phenomenon in the CCD camera, especially when the integration time is 23s, the error between adjacent points is significantly reduced, and the CCD enters the saturation zone.

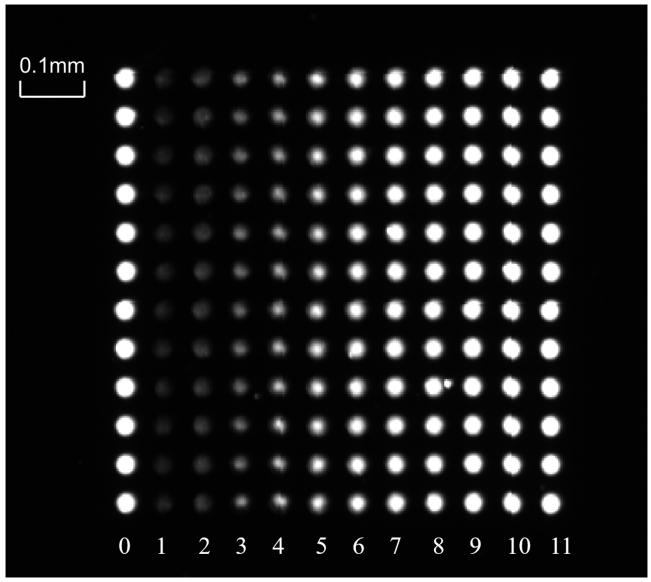

Fig. 5. Grayscale image scanned from Beijing CapitalBio Nanobrite™ Cy3 calibration chip at the integration time of 30 s.

During the dataset processing of MLP, we extracted one point as the test set from three points while the other two points as the training set, sequentially. This method could ensure that the test set and the training set are evenly distributed, and we would obtain the test set and training set under a ratio of 1 : 2.

As is well known, the relative error has a higher sensitivity to error compared to absolute error, especially when the error between predicted value and actual value is small, the absolute error will ignore this proportional error. Meanwhile, the relative error is a dimensionless ratio that can be compared across different units and scales. Therefore, we use the relative error as the evaluation index in the comparative experiments.

B. Curve Fitting By LSA

By LSA fitting, we can assume that the mathematical model between the integration time (exposure time) of the CCD taking image in the CCD scanner, denoted as t, and the gray value of the output image can be expressed as follows

$$Grayvalue = k_0 + k_1 H_t^1 + k_2 H_t^2 + \ldots + k_n H_t^n \tag{35}$$

where H_t expressed in (4), while n denoted as the order of polynomial fitting.

The fitting curve of LSA can be obtained by solving each unknown parameter in (35). In order to obtain a higher fitting accuracy, we evaluated standard curves with fitting order at 7, 8, and 9 by LSA. When we use the dataset as shown in the sixth column like Fig. 5 while the integration time from 1 s to 30 s, we can fit the standard curve and the relative error of curve as shown in Fig. 6, the evaluation index values for fitting curves are shown in Table II.

TABLE I
DATA VALUES AND THE DIFFERENCE BETWEEN ADJACENT POINTS

Integration time	Grayscale value	The difference between adjacent points
1	2878.9	-
2	5750.1	2871.2
3	8619.3	2869.2
4	11467	2847.7
5	14472	3005
6	16805	2333
7	20211	3406
8	23084	2873
9	25957	2873
10	28387	2430
11	31449	3062
12	34191	2742
13	36837	2646
14	39505	2668
15	41877	2372
16	44411	2534
17	46921	2510
18	49181	2260
19	52501	3320
20	54865	2364
21	57105	2240
22	59103	1998
23	**61161**	**2058**
24	62454	1293
25	63780	1326
26	64517	737
27	64890	373
28	65195	305
29	65319	124
30	65389	70

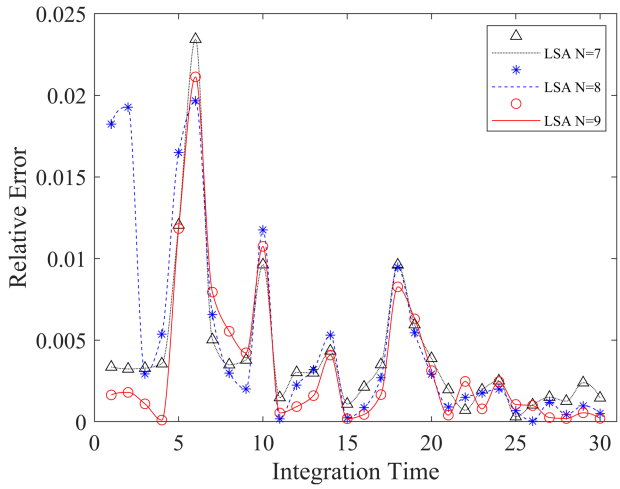

Fig. 6. The relative error of LSA fitting curve at N = 7/8/9, where black represents the relative error of LSA (N = 7) fitting curve, blue represents the relative error of LSA (N = 8) fitting curve, and red represents the relative error of LSA (N = 9) fitting curve.

TABLE II
FITTING RESULTS OF LSA

Fitting Method	Maximum relative error	Standard deviation of relative error
LSA(N=7)	2.34%	0.45%
LSA(N=8)	1.96%	0.60%
LSA(N=9)	2.11%	0.46%

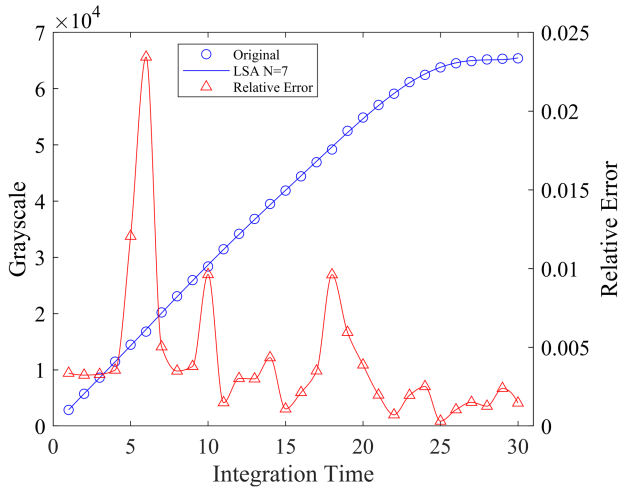

Fig. 7. The LSA fitting curve and the relative error at N = 7, where the blue circle represents the original data, the blue curve represents the fitting curve, the red triangle represents the relative error at each point, and the red line represents the relative error of the fitting curve.

From Fig. 6 and Table II, a conclusion could be drawn that the relative errors of the fitting curve do not change obviously when N is taken to be 7, 8 and 9 in the LSA fitting. Therefore, it can be assumed that there is no significant change in the LSA fitting curve when N is greater than 7. So we could choose to fit the standard curve by LSA at N = 7, and this fitting curve and its relative errors are shown in Fig. 7.

Obviously, the maximum relative error of the LSA fitting curve is found in the region of smaller gray level of the image, and it can be seen from the experiment that the LSA use the constraint of minimization of the SSE, which cannot effectively minimized the relative error of the fitting curve. This drawback will greatly affect the fitting accuracy of the CCD scanner's operating curve.

Meanwhile, the LSA prioritizes fitting values with significant absolute errors, which can lead to neglecting some values with smaller absolute errors, resulting in significant relative errors in the fitted curve for individual data and causing oscillation in the relative error of the fitted curve.

C. Curve Fitting of WLS and PLS

Due to the significant relative error of LSA in areas with smaller values, we set the weight of the first six data points to 10 and the weight of the remaining data points to 1. At the same time, we set its penalty coefficient to 0.01 during the PLS

TABLE III
FITTING RESULTS OF WLS AND PLS

Fitting Method	Fit order	Maximum relative error	Standard deviation of relative error
WLS	N=7	1.71%	0.46%
	N=8	1.71%	0.47%
	N=9	1.70%	0.50%
PLS	N=7	2.40%	0.57%
	N=8	2.22%	0.51%
	N=9	2.26%	0.53%

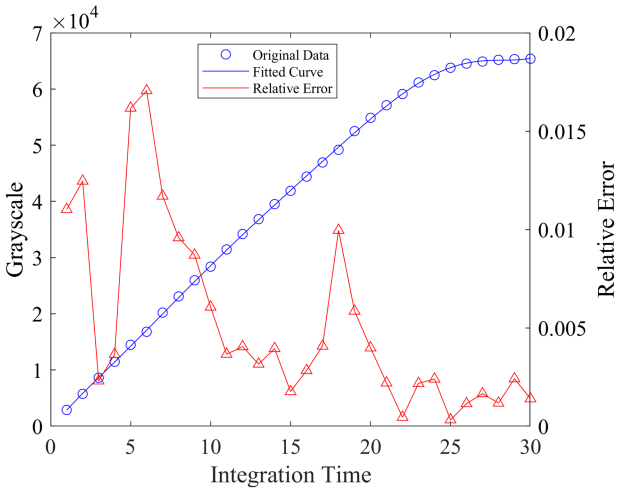

Fig. 8. The WLS fitting curve and the relative error at N = 7, where the blue circle represents the original data, the blue curve represents the fitting curve, the red triangle represents the relative error at each point, and the red line represents the relative error of the fitting curve.

fitting process. Then, we used WLS and PLS to fit the data at N = 7, 8, and 9, respectively, while the maximum relative error and standard deviation of the fitted curves are shown in Table III.

From Table III, we can conclude that there is no significant change in the maximum relative error of the fitting curves for both WLS and PLS when N is greater than 7. Therefore, we can use the WLS and PLS fitting curves at N = 7 for comparative experiments.

Subsequently, the fitting curve and relative error of WLS at N = 7 are shown in Fig. 8, and the fitting curve and relative error of PLS at N = 7 are shown in Fig. 9.

D. Multi-Layer Perceptron Curve Fitting

The structure of MLP is showed in Fig. 4, which is configured with an input layer, a hidden layer and an output layer, and each neuron in hidden layer is serving its specific purpose. The fitting experiments of the standard curves were performed employing the sigmoid function as the activation function of the hidden layer with the learning rate of 0.1 and the training round of 40000 times in order to minimize the SSE.

During the MLP processing, the Fig. 10 traces the SSE stabilization process for both the training and test sets. Subsequently, the Fig. 11 illustrates the fitting curves and relative errors.

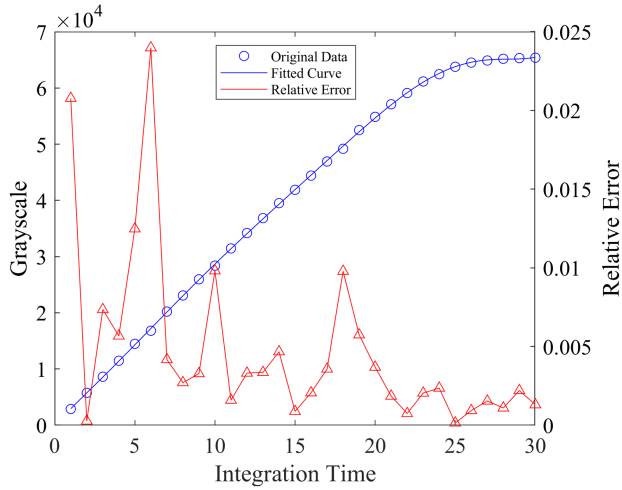

Fig. 9. The PLS fitting curve and the relative error at N = 7, where the blue circle represents the original data, the blue curve represents the fitting curve, the red triangle represents the relative error at each point, and the red line represents the relative error of the fitting curve.

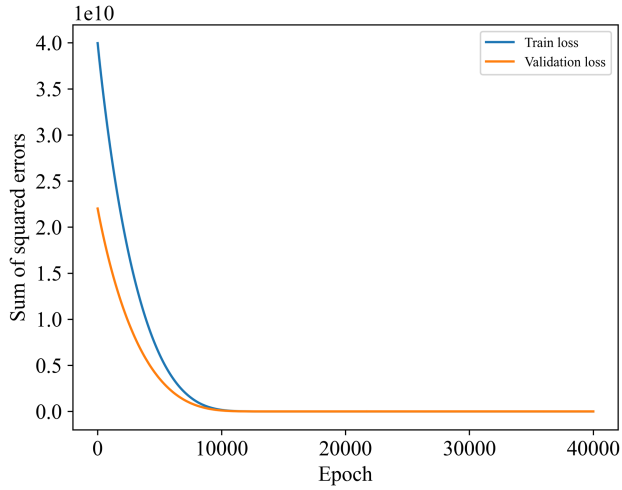

Fig. 10. The SSE in test and training sets during the MLP processing by SSE minimization (after 40 000 rounds), where the blue curve represents the loss on the training set, and the orange curve represents the loss on the validation set.

Unfortunately, even though we tried our best to minimize the SSE, we still observed a maximum relative error of 3.32% and a standard deviation of 0.67% for the MLP fitting curve. Notably, a significant relative error still persists, particularly in the low detection region of the image, even when the standard curve is fitted by the MLP method with the constraint of SSE minimization. Therefore, we can conclude that the SSE minimization constraint is not effective in reducing the maximum relative error of the fitting curves, regardless of LSA or MLP method. In order to minimize the relative error of the fitting curve, we adjusted the constraint condition to the maximum relative error as the optimization constraint condition, and retrained the MLP neural network.

As depicted in Fig. 12, the processing trajectories are also stabilized for both the training and test sets. We can conclude that the relative error of the standard curve fitted with the MLP under

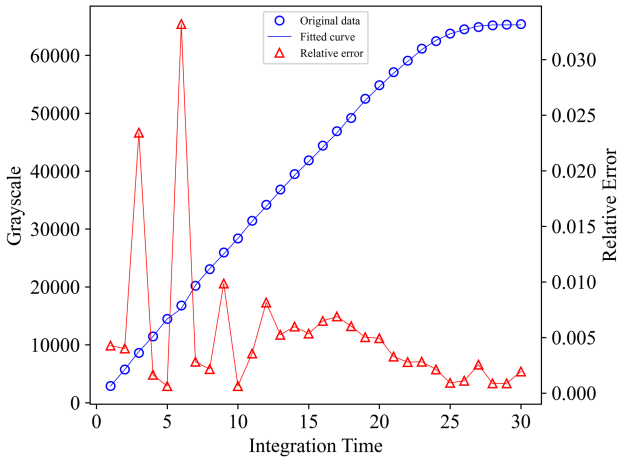

Fig. 11. The MLP fitting curve and the relative error by SSE minimization (after 40 000 rounds), where the blue circle represents the original data, the blue curve represents the fitting curve, the red triangle represents the relative error at each point, and the red line represents the relative error of the fitting curve.

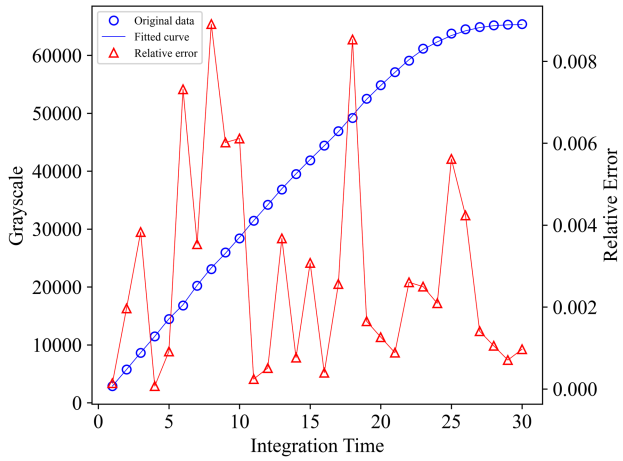

Fig. 13. The MLP fitting curve and relative error based on relative errors minimization (after 40 000 rounds), where the blue circle represents the original data, the blue curve represents the fitting curve, the red triangle represents the relative error at each point, and the red line represents the relative error of the fitting curve.

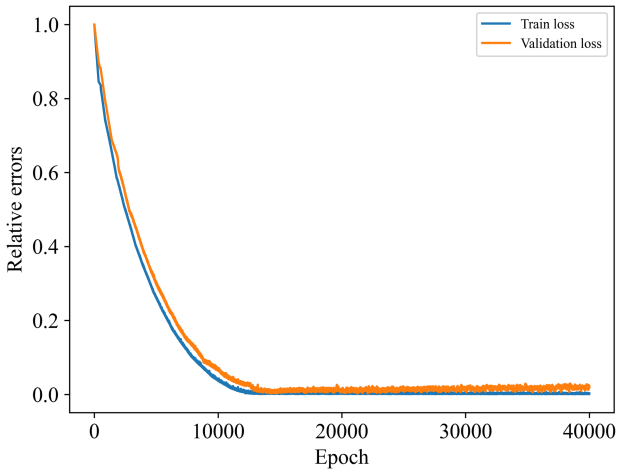

Fig. 12. The relative error in test and training sets during MLP training based on relative error minimization, where the blue curve represents the loss on the training set, and the orange curve represents the loss on the validation set.

the constraint of minimizing the relative error is very small. And as shown in Fig. 13, the maximum relative error is only 0.89% while the standard deviation of the relative error is 0.25%.

E. Comparison of Different Curve Fitting Methods

We used the maximum relative error and the standard deviation of the relative error as the evaluation indexes. As shown in Table IV, we can find that even if the LAS is fitted at N = 7, the maximum relative error of the standard curve fitted by LSA is still as high as 2.34%, while the standard deviation of its relative error is also as high as 0.45%, so the LSA does not constrain the relative error very well in the fitting. In addition, there is a large relative error in the low detection region of the image in Fig. 7, which will have a significant impact on the measurement accuracy of our scanner. We also used WLS and PLS to fit the data, but their experimental results were also unsatisfactory.

TABLE IV
COMPARISON OF CURVE-FITTING EXPERIMENTAL RESULTS

Fitting Method	Maximum relative error	Standard deviation of relative error
LSA(N=7)	2.34%	0.45%
WLS(N=7)	1.71%	0.46%
PLS(N=7)	2.40%	0.57%
MLP+SSE	3.32%	0.67%
MLP+relative error	0.89%	0.25%

And this unfavorable effect of LAS also appears in the MLP fitting by constraining with SSE minimization, leading to poor performance in Fig. 11. However, the MLP with the relative error minimization constraint can well reduce the maximum relative error to only 0.89%, while the standard deviation of the relative error is 0.25%. At the same time, the relative errors are also smaller in areas where the fluorescence image has a smaller detection.

In Table IV, the results of these experiments can be found that the standard curve fitted by the MLP with the relative error minimization constraint has a significant improvement in the accuracy of the CCD scanner.

V. CONCLUSION

Due to the characteristics of semiconductors, CCD sensors are not immune to the saturation phenomena, which make the nonlinear relationship between the photoelectric response and the light intensity collected by CCD. This nonlinear characteristic poses a challenge to standard curve fitting for CCD scanners. Considering that a large relative error will greatly affect the measurement accuracy of the CCD scanner, we use a high order polynomial for standard curve fitting at first. However, the LSA which is a commonly fitting algorithm has a large relative error

when fitting the standard curve to the CCD sensor, especially in the low detection region of the scanner image. Even in the case of higher-order fitting (N = 7), the maximum relative error of the fitting curve by LSA is still as high as 2.34%, and the standard deviation of the relative errors was 0.45%. At the same time, WLS and PLS cannot significantly reduce the maximum relative error, which will affect the accuracy of the scanner. Therefore, we propose an MLP neural network algorithm with the relative error minimizing for standard curve fitting to overcome the nonlinear effects of CCD sensors.

The experimental results show that the maximum relative error and the standard deviation of the relative errors for the curve fitted by the MLP with the minimization of the relative error as the constraint are smaller than the other two methods. And its maximum relative error was dropped to only 0.89% while the standard deviation of the relative error was 0.25%, so it can be seen that this method of MLP with the relative error minimization is very important for studying standard curve fitting for quantitative measurement instruments.

Nevertheless, there are still some challenges to be further solved for MLP-based standard curve fitting to improve the quantitative detection accuracy of CCD scanners, including (1) developing an effective dataset expansion method to solve the problem of dataset size in curve fitting; (2) achieving a suitable method for labeling these datasets with high precision, and (3) determining a critical saturation point of a CCD sensor to eliminate unfavorable regions. These endeavors will contribute to improve the performance of standard curve fitting for CCD scanner.

ACKNOWLEDGMENT

The authors would like to thank the scientific team of Key Lab of Medical Instrumentation and Pharmaceutical Technology of Fujian Province for providing the experimental supports, and also thank the help from Taipu Beijing.

REFERENCES

[1] R. S. Sengar, A. K. Upadhyay, and B. Jain, "Deep learning aided small-sized portable fluorescence biochip reader," *IEEE Trans. Instrum. Meas.*, vol. 71, May 2022, Art. no. 2507709.

[2] G. M. Aparna and K. K. R. Tetala, "Recent progress in development and application of DNA, protein, peptide, glycan, antibody, and aptamer microarrays," *Biomolecules*, vol. 13, no. 4, Mar. 2023, Art. no. 602.

[3] Z. Gan et al., "Highly sensitive Cy3 fluorescence detection method for microarray based on CCD and LED," *IEEE Trans. Instrum. Meas.*, vol. 72, Sep. 2023, Art. no. 5028112.

[4] Z. Liu, W. Liu, and Z. Han, "A high-precision detection approach for catenary geometry parameters of electrical railway," *IEEE Trans. Instrum. Meas.*, vol. 66, no. 7, pp. 1798–1808, Jul. 2017.

[5] Z. Gan et al., "Multilevel segmentation optimized by physical information for gridding of microarray images," *IEEE Access*, vol. 7, pp. 32146–32153, 2019.

[6] Z. Liu, Y. Lyu, L. Wang, and Z. Han, "Detection approach based on an improved faster RCNN for brace sleeve screws in high-speed railways," *IEEE Trans. Instrum. Meas.*, vol. 69, no. 7, pp. 4395–4403, Jul. 2020.

[7] W. Li et al., "Development of a low-cost detection method for miRNA microarray," *Acta Biochimica et BiophysicaSinica*, vol. 42, no. 4, pp. 296–301, Apr. 2010.

[8] F. Erfurth et al., "Two-laser, large-field hyperspectral microarray scanner for the analysis of multicolor microarrays," *Anal. Chem.*, vol. 80, no. 20, pp. 7706–7713, Sep. 2008.

[9] N. Zeng, P. Wu, Z. Wang, H. Li, W. Liu, and X. Liu, "A small-sized object detection oriented multi-scale feature fusion approach with application to defect detection," *IEEE Trans. Instrum. Meas.*, vol. 71, 2022, Art. no. 3507014.

[10] J. Ren et al., "Establishment and application of CCD radiation response function matrix," *Opt. Precis. Eng.*, vol. 20, no. 5, pp. 957–962, May 2012.

[11] H. Faraji and W. J. MacLean, "CCD noise removal in digital images," *IEEE Trans. Image Process.*, vol. 15, no. 9, pp. 2676–2685, Sep. 2006.

[12] J. Luo et al., "Analysis and correction of smeared image from interline-transfer CCD in beam quality measurement," *IEEE Photon. J.*, vol. 14, no. 6, Dec. 2022, Art. no. 7863908.

[13] B. A. Berg, "Least square fitting with one explicit parameter less," *Comput. Phys. Commun.*, vol. 200, pp. 254–258, Jan. 2016.

[14] E. López-Rubio et al., "A fast robust geometric fitting method for parabolic curves," *Pattern Recognit.*, vol. 84, pp. 301–316, Jul. 2018.

[15] G. Rémi, "Should penalized least squares regression be interpreted as maximum a posteriori estimation?," *IEEE Trans. Signal Process.*, vol. 59, no. 5, pp. 2405–2410, May 2011.

[16] F. B. M. Suah, M. Ahmad, and M. N. Taib, "Optimisation of the range of an optical fibre pH sensor using feed-forward artificial neural network," *Sensor Actuators B: Chem.*, vol. 90, pp. 175–181, Apr. 2003.

[17] F. Hu et al., "A human body posture recognition algorithm based on BP neural network for wireless body area networks," *China Commun.*, vol. 13, no.no. 8, pp. 198–208, Aug. 2016.

[18] Y. Li et al., "Fitting analysis and research of measured data of SAW micro-pressure sensor based on BP neural network," *Measurement*, vol. 155, pp. 107533–107538, Jan. 2020.

[19] L. Yi, Y. Wu, A. Tolba, T. Li, S. Ren, and J. Ding, "SA-MLP-Mixer: A compact All-MLP deep neural net architecture for UAV navigation in indoor environments," *IEEE Internet Things J.*, vol. 11, no. 12, pp. 21359–21371, Jun. 2024, doi: 10.1109/JIOT.2024.3359662.

[20] D. Wang and L. Wang, "On OCT Image classification via deep learning," *IEEE Photon. J.*, vol. 11, no. 5, Oct. 2019, Art. no. 3900714.

[21] G. Li et al., "A new artificial lateral line attitude perception method based on mixed activation function-multilayer perceptron (MAF-MLP)," *Ocean Eng.*, vol. 288, Oct. 2023, Art. no. 116100.

[22] F. Rodríguez et al., "Very short-term temperature forecaster using MLP and N-nearest stations for calculating key control parameters in solar photovoltaic generation," *Sustain. Energy Technol. Assessments*, vol. 45, Feb. 2021, Art. no. 101085.

[23] T. Sathish et al., "Characteristics estimation of natural fibre reinforced plastic composites using deep multi-layer perceptron (MLP) technique," *Chemosphere*, vol. 337, Jun. 2023, Art. no. 139346.

[24] N. Kretschy, M. Sack, and M. M. Somoza, "Sequence-dependent fluorescence of Cy3- and Cy5-labeled double-stranded DNA," *Bioconjugate Chem.*, vol. 27, no. 3, pp. 840–848, Mar. 2016.

[25] J. M. Obliosca, P. C. Wang, and F. G. Tseng, "Probing quenched dye fluorescence of Cy3-DNA-Au-nanoparticle hybrid conjugates using solution and array platforms," *J. Colloid Interface Sci.*, vol. 371, no. 1, pp. 34–41, Apr. 2012.

[26] P. Sawangsang, C. Buranachai, and C. Punwong, "Excited state free energy calculations of Cy3 in different environments," *J. Phys. D: Appl. Phys.*, vol. 48, no. 20, Apr. 2015, Art. no. 205401.

[27] A. Nohtomi et al., "Observation of water luminescence for diagnostic 120-kV X-rays by using PMT and CCD camera," *Nucl. Instruments Methods Phys. Res. Sect. A: Accelerators, Spectrometers, Detectors Assoc. Equip.*, vol. 988, Dec. 2020, Art. no. 164935.

[28] K. Azil et al., "A faster and accurate optical water turbidity measurement system using a CCD line sensor," *Optik*, vol. 231, Feb. 2021, Art. no. 166412.

[29] Z. Gan, M. Du, Y. Gao, B. Xiong, and P. Yang, "Measurement of CCD light intensity response characteristics based on LED," *China Meas. Test*, vol. 42, no. 12, pp. 52–57, Dec. 2016.

[30] M. Akhlaq and T. R. Sheltami, "RTSP: An accurate and energy-efficient protocol for clock synchronization in WSNs," *IEEE Trans. Instrum. Meas.*, vol. 62, no. 3, pp. 578–589, Mar. 2013.

[31] L. Sun, "Signal-dependent noise parameter estimation of hyperspectral remote sensing images," *Spectrosc. Lett.*, vol. 48, no. 10, pp. 717–725, Nov. 2014.

[32] G. A. Mohammed and M. Hou, "Optimization of active muscle force-length models using least squares curve fitting," *IEEE Trans. Biomed. Eng.*, vol. 63, no. 3, pp. 630–635, Mar. 2016.

[33] P. Wu et al., "AGGN: Attention-based glioma grading network with multi-scale feature extraction and multi-modal information fusion," *Comput. Biol. Med.*, vol. 152, Jan. 2023, Art. no. 106457.